Received: 23 May 2023 | Revised: 3 May 2024 | Accepted: 26 May 2024

DOI: 10.1002/qj.4785

Quarterly Journal of the Royal Meteorological Society RMetS

RESEARCH ARTICLE

An analytical model for daily-periodic slope winds. Part 1: Surface radiation budget

Mattia Marchio[1,2] | **Sofia Farina**[1,2] | **Dino Zardi**[1,2]

[1]Atmospheric Physics Group, Department of Civil, Environmental and Mechanical Engineering (DICAM), University of Trento, Trento, Italy

[2]Center Agriculture Food Environment (C3A), University of Trento, Trento, Italy

Correspondence
Mattia Marchio and Dino Zardi, Department of Civil, Environmental and Mechanical Engineering, University of Trento, Via Mesiano 77, Trento 38122, Italy.
Email: mattia.marchio@unitn.it, dino.zardi@unitn.it

Funding information
European Union "NextGenerationEU" and Italian Ministry of University and Research, Grant/Award Numbers: Prot.2022NEWP4J, CUP E 53 D 23004450006

Abstract

This article presents an analytical model for calculating representative daily-periodic cycles of net surface radiation on a slope with any angle α ($0° \leq \alpha \leq 90°$) and orientation, at any latitude and elevation (up to 2500 m), and for all seasons. Starting from the basic equations for estimating the daytime direct and diffuse components of the incoming solar radiation at the Earth's surface under clear-sky conditions, a Fourier series expansion is derived to get an overall daily-periodic expression, that is, covering both daytime and nighttime, which does not require data from observations, differently from most models available in the literature. Among various possible applications, this formulation is preliminary to evaluating the radiation and energy budgets driving daily-periodic wind systems on a simple slope, as reproduced by the model presented in Part 2.

KEYWORDS

clear-sky, daily cycle, Fourier series expansion, mountainous terrain, net radiation

1 | INTRODUCTION

The evaluation of the radiation budget at the Earth's surface, the main driver of the surface energy budget, is of utmost importance for a variety of applications (e.g., Castelli *et al.*, 2014). In particular, over complex terrain, the diurnal cycle of net surface radiation controls, through the surface sensible heat flux, the onset and development of daily-periodic local winds. They are named *thermally driven*, as they are promoted by surface heating or cooling (Serafin & Zardi, 2011; Serafin *et al.*, 2018; Whiteman, 2000; Zardi & Whiteman, 2013). These flows are associated with turbulent exchanges of mass, heat, and momentum between the surface and the atmosphere, and concur to characterize a variety of local microclimates typical of mountain areas (Whiteman *et al.*, 1989). A series of processes in these areas are controlled by alternating regimes associated with the above winds, ranging from land–atmosphere exchanges affecting the hydrological cycle, such as evapotranspiration (e.g., Allen *et al.*, 2006; Hargreaves & Samani, 1982; Mokhtari *et al.*, 2018) and snow melting (Seyednasrollah *et al.*, 2013), transport of passive tracers, including both biogenic species (such as pollens and spores: e.g., Zhang *et al.*, 2017) and harmful compounds (e.g., pollutants and pesticides: De Wekker *et al.*, 2018; Giovannini *et al.*, 2020; Urgnani *et al.*, 2022), renewable energy sources (Laiti *et al.*, 2018; Lindauer *et al.*, 2017), the energetic budget of buildings (Kirkpatrick & Winn, 1984; Zonato *et al.*, 2021), as well as numerical weather predictions (Senkova *et al.*, 2007) and the study of climate change, through the close relationship between net radiation and surface air temperature (Tscholl *et al.*, 2021).

Among the various categories of thermally driven winds, the simplest ones are slope winds (Farina & Zardi, 2023), that is, those developing over simple slopes

and characterized by an upslope phase during daytime and a downslope phase during nighttime, separated by transitional phases at sunrise and sunset (Farina *et al.*, 2023).

The evaluation of incoming radiation over mountainous terrain is complicated by different factors. First of all, measurements are quite rare, as routinely operated surface weather stations rarely include net radiometers. Furthermore, in complex terrain areas such stations are fewer, since their installation and maintenance is difficult (Laiti *et al.*, 2018). Over flat terrain, the spatial correlation scale of surface radiation is quite large, and hence measurements are representative of rather extended surroundings. Instead, over complex terrain, local topography strongly affects the amount of radiation reaching different portions of the surface through inclination and shading effects (Allen *et al.*, 2006; Emeis *et al.*, 2018). To account for that, various models were proposed in the literature for estimating net radiation under different conditions. However, many of these models require input data from observations, which can result in misleading information if measurements are not taken close enough to the target area (e.g., Tscholl *et al.*, 2021).

For the elementary case of a simple slope, Whiteman and Allwine (1986) proposed an analytical model for estimating the daytime cycle of incoming extraterrestrial solar radiation for every day of the year, latitude, slope angle, and orientation, between local sunrise and sunset times, based on an iterative procedure. Allen *et al.* (2006) extended the results of Whiteman and Allwine (1986), improving the evaluation of sunrise and sunset timings for the slope and including a formulation accounting for atmospheric transmittance, diffusion, and reflection from the atmosphere and topography. Similarly, Seyednasrollah *et al.* (2013) used the simplified formulation for the atmospheric transmittance suggested by Hottel (1976) to estimate the daytime cycle of incoming solar radiation, for every day of the year, latitude, slope angle, and orientation, but evaluating sunrise and sunset times as for horizontal terrain. Remarkably, all the above analytical models provide expressions for incoming shortwave radiation only for daytime.

The ultimate goal of the present research is to provide a comprehensive model covering the whole daily cycle of local, thermally driven circulations developing over simple slopes as a consequence of daytime heating and nighttime cooling (e.g., Giovannini *et al.*, 2017; Whiteman, 2000). To this purpose, the whole daily cycle of air temperature at the surface is needed as a realistic forcing. Hence, a fundamental step is the derivation of a full daily-periodic analytical model describing the radiative input. Accordingly, the objective of Part 1 is to obtain a simplified analytical model for the estimation of the full daily-periodic cycle (i.e., covering both daytime and nighttime) of net radiation, locally valid for virtually any slope.

The model presented here estimates both incoming direct and diffuse shortwave radiation by means of (truncated) Fourier series expansions, taking into account local terrain characteristics (slope angle and orientation), as well as astronomical input concerning the inclination of Sun rays with respect to the underlying terrain (according to latitude and season) and the clear-sky atmospheric transmittance proposed by Hottel (1976). Furthermore, outgoing shortwave radiation is estimated by means of an average surface albedo, and the net longwave radiation at the surface is computed through a suitable daily cycle of surface and near-surface temperature. The main simplification consists of neglecting the incoming radiation reflected by the surrounding topography, consistently with the idealized approximation of an infinitely extended and isolated slope, implied for Part 2 of this article (Marchio *et al.*, 2024).

The article is organized as follows. Section 2 reviews the equations required for computing the extraterrestrial solar radiation and estimating the atmospheric transmittance on sloping surfaces. The series expansion used to derive the whole daily cycle of net radiation is also presented in this section. Moreover, the model performance is evaluated along with the accuracy of the approximation implied by the model, depending on the number of harmonics included. Section 2 also shows how the model reproduces the daily cycles of net radiation, once albedo and longwave radiation are taken into account. Discussions and conclusions are briefly summarized in Section 3, while further details on the approximations implied in the atmospheric transmittance model are accounted for in the Appendix.

2 | FORMULATION OF THE MODEL

2.1 | Surface radiation budget

Let R_{net} indicate the net all-wave radiation at the surface:

$$R_{net} = K_{net} + L_{net}, \tag{1}$$

where $K_{net} = K_{in} + K_{out} = (1 - A)K_{in}$ is the net shortwave radiation, resulting from the unbalance between incoming shortwave radiation K_{in} and outgoing shortwave radiation $K_{out} = -AK_{in}$, with A being the surface albedo, that is, the fraction of incoming solar radiation reflected by the ground. The incoming shortwave radiation is composed of both direct K_{dir} and a diffuse K_{dif} components: $K_{in} = K_{dir} + K_{dif}$. The former depends on the extraterrestrial solar radiation K_{extr} and on the atmospheric transmittance (as shown below).

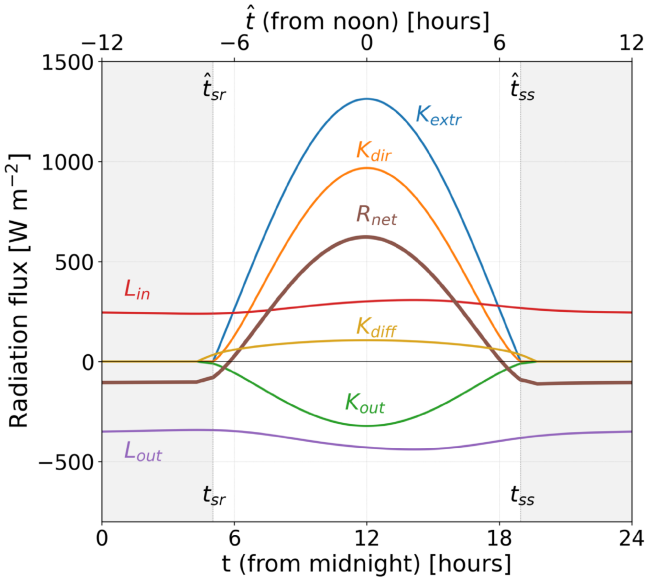

FIGURE 1 Daily cycle of net radiation at the surface and its components for a typical clear-sky summer day (June 21, DOY = 172) at a latitude of 45°N, for a south-oriented slope, with a slope angle of 15° at an elevation of 1500 m. The net all-wave radiation (brown curve) can be considered daily-periodic. Here t and $\hat{t}$ denote the local time, evaluated from midnight and from noon respectively, while t_{SR} ($\hat{t}_{SR}$) and t_{SS} ($\hat{t}_{SS}$) are the sunrise and sunset hours, respectively. K_{extr} is the extraterrestrial incoming solar radiation (Equation 4), K_{dir} and K_{dif} are the direct and diffuse components of the incoming radiation reaching the surface (Equations 12 and 17, respectively). K_{out} is the outgoing shortwave radiation, computed using an albedo of $A = 0.3$. LW_{out} and LW_{in} are the incoming and outgoing longwave fluxes (Equations 20 and 21 respectively), with emissivities $\epsilon_s = 0.95$ and $\epsilon_a = 0.7$. The daily cycle of surface temperature was computed from Equation (A1), using four harmonics with a mean temperature of 290 K and the following amplitudes and phases: $\Delta T_1 = 9$ K, $\Delta T_2 = 2$ K, $\Delta T_3 = 0.5$ K, $\Delta T_4 = 0.2$ K, $\phi_1 = 1.05$ rad, $\phi_2 = 0.9$ rad, $\phi_3 = -2.26$ rad, and $\phi_4 = -2.27$ rad.

Similarly, the net longwave radiation $L_{net} = L_{in} + L_{out}$ results from the unbalance between the incoming longwave radiation L_{in} and the outgoing longwave radiation L_{out}. Under clear-sky situations, both of these undergo a daily cycle, resulting from the daily cycle of surface and near-surface temperatures (details in the next section). An example of a typical daily radiation cycle for a midsummer day is shown in Figure 1. Hence, Equation (1) can be rewritten as

$$R_{net} = (1 - A)\ (K_{dir} + K_{dif}) + L_{net}. \tag{2}$$

2.2 | Direct incoming radiation

The amount of direct solar radiation reaching the surface K_{dir} can be evaluated from the extraterrestrial incoming radiation K_{extr} as

$$K_{dir} = K_{extr}\tau, \tag{3}$$

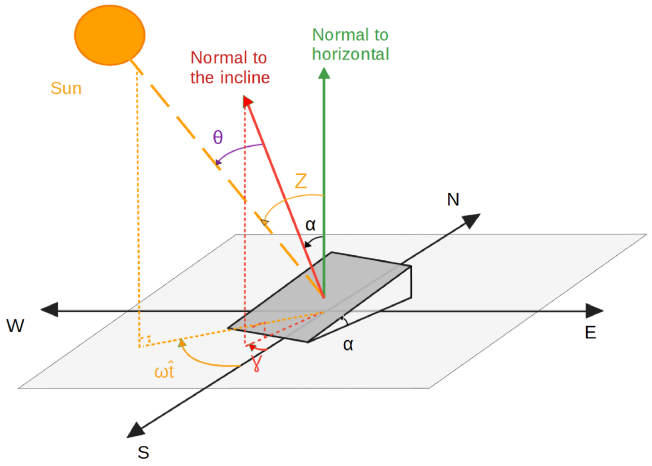

FIGURE 2 Schematic of incoming solar radiation on a surface with slope angle α: θ is the solar incidence angle (Equation 6), γ is the aspect (with 0° corresponding to a south-facing slope), $\omega\hat{t}$ is the hour angle, and Z is the solar zenith angle (Equation 7).

where τ is the atmospheric transmittance (Kreith & Kreider, 2011), and K_{extr} can be computed as in Allen *et al.* (2006):

$$K_{extr} = R_s \cos\theta, \tag{4}$$

where $R_s = G_{sc} d^{-2}$ is the extraterrestrial solar radiation at the top of the atmosphere, $G_{sc} = 1366.1\,\mathrm{W{\cdot}m^{-2}}$ the solar constant, d the distance between the Earth and the Sun in astronomical units, and $\cos\theta$ the cosine of the solar incidence angle θ (i.e., the angle between the Sun's rays and the vector normal to the inclined surface, as in Figure 2).

Over flat terrain, the incoming solar radiation depends on geographical and seasonal factors only, while over a slope the solar incidence angle also depends on the slope angle α and orientation γ (Garnier & Ohmura, 1968):

$$\begin{aligned}\cos\theta = {} & (\sin\phi\cos\alpha - \cos\phi\sin\alpha\cos\gamma)\sin\delta \\ & + (\cos\phi\cos\alpha + \sin\phi\sin\alpha\cos\gamma)\cos\delta\cos(\omega\hat{t}) \\ & + \cos\delta\sin\gamma\sin\alpha\sin(\omega\hat{t}),\end{aligned} \tag{5}$$

where ϕ is the latitude, α is the slope angle, γ is the slope orientation or aspect ($\gamma = 0°$ for a slope facing south, 180° facing north, and ±90° facing west and east respectively), and δ is the solar declination angle. Here, $\omega\hat{t}$ is the hour angle ($\omega = 7.272 \times 10^{-5}\,\mathrm{s^{-1}}$ is the angular frequency associated with the daily period and $\hat{t} = t - 12\,\mathrm{h}$, where t is the local time). For a horizontal surface ($\alpha = 0$), the solar incidence angle reduces to the solar zenith angle Z:

$$\cos Z = \sin\phi\sin\delta + \cos\phi\cos\delta\cos(\omega\hat{t}). \tag{6}$$

The scheme proposed by Hottel (1976) allows computation of the atmospheric transmittance in clear-sky conditions as

$$\tau = \tau_0 + \tau_1 \exp\left(-\frac{k}{\cos Z}\right), \tag{7}$$

where τ_0, τ_1, and k are coefficients depending on terrain altitude and atmospheric optical properties, determined on the basis of typical values for the content of water vapor, ozone, and aerosol in the atmosphere. This model has been extensively used in the literature for a series of applications where an accurate estimate of transmittance was required under various atmospheric conditions. Notice, however, that the approximations implied in its formulation were admittedly optimized in view of keeping the model as simple as possible, and at the same time containing its inaccuracy within 0.3% of the value of τ that could be evaluated from more rigorous, but more complex calculations. However, such an accuracy is granted by Hottel (1976) only for altitudes up to 2500 m ASL. Strictly speaking, the term $1/\cos Z$ represents the relative optical mass only for a plane parallel atmosphere. Indeed, neglecting the Earth's curvature and the refraction of the real atmosphere implies an inaccuracy of 0.25% at $Z = 60°$, increasing to 10% at $Z = 85°$ (Iqbal, 1983). However, Hottel's formulation compensates for these errors deriving the coefficients from a least-square-error best-fitting procedure for different values of the air mass.

Combining Equations (3) to (5), and (7), the incoming radiation on a slope can be rewritten as

$$\begin{aligned} K_{\mathrm{dir}}(\hat{t}) = \frac{G_{\mathrm{sc}}}{d^2}\Big[&(\sin\phi\cos\alpha - \cos\phi\sin\alpha\cos\gamma)\sin\delta \\ &+ (\cos\phi\cos\alpha \\ &+ \sin\phi\sin\alpha\cos\gamma)\cos\delta\cos(\omega\hat{t}) \\ &+ \cos\delta\sin\gamma\sin\alpha\sin(\omega\hat{t})\Big] \\ &\times\left(\tau_0 + \tau_1\cdot\exp\left(-\frac{k}{\cos Z}\right)\right). \end{aligned} \tag{8}$$

Since the values of $\cos Z$ in the exponential term must be non-negative, the above formula makes sense only when computed between local sunrise ($\hat{t}_{\mathrm{SR}}$) and sunset ($\hat{t}_{\mathrm{SS}}$) times. Over horizontal terrain, these times can be easily computed from latitude and season alone. Instead, for non-horizontal surfaces, the computation is less trivial, as extensively discussed by Iqbal (1983) and Allen *et al.* (2006). In particular, over a slope they depend on slope angle and exposure. Expressions for $\hat{t}_{\mathrm{SR}}$ and $\hat{t}_{\mathrm{SS}}$ in such a case are reported in the supplementary material. Notice, that at latitudes higher than the polar circles, there are times of the year when the sun never rises or never sets, requiring further constraints when computing sunrise and sunset times.

In view of expressing the 24-h periodicity only through sine or cosine terms of the hour angle, we approximate the exponential term in Equation (7) as

$$\begin{aligned} &\exp\left(-\frac{k}{\cos Z}\right) \\ &\quad\simeq \exp\left(-\frac{k}{\cos(\phi-\delta)}\right)\frac{1}{F_{\mathrm{c}}}(\cos Z + c_3\cos 3Z), \end{aligned} \tag{9}$$

where c_3 is a coefficient, the derivation of which is explained in the Appendix, and

$$F_{\mathrm{c}} = \cos(\phi-\delta) + c_3\cos(3(\phi-\delta)) \tag{10}$$

is a normalization factor ensuring that the approximated expression attains the exact maximum value at $\hat{t} = 0$. Further details on the formulation of Equation (9) and its level of accuracy are discussed thoroughly in the Appendix.

Substituting Equation (9) into Equation (8) and isolating likewise terms, we obtain

$$\begin{aligned} K_{\mathrm{dir}}(\hat{t}) = K_0 &+ K_{1\mathrm{C}}\cos(\omega\hat{t}) + K_{1\mathrm{S}}\sin(\omega\hat{t}) \\ &+ K_{2\mathrm{C}}\cos(2\omega\hat{t}) + K_{2\mathrm{S}}\sin(2\omega\hat{t}) \\ &+ K_{3\mathrm{C}}\cos(3\omega\hat{t}) + K_{3\mathrm{S}}\sin(3\omega\hat{t}) \\ &+ K_{4\mathrm{C}}\cos(4\omega\hat{t}) + K_{4\mathrm{S}}\sin(4\omega\hat{t}). \end{aligned} \tag{11}$$

The full expressions to calculate the coefficients K_0, $K_{1\mathrm{C}}$, $K_{1\mathrm{S}}$, $K_{2\mathrm{C}}$, $K_{2\mathrm{S}}$, $K_{3\mathrm{C}}$, $K_{3\mathrm{S}}$, $K_{4\mathrm{C}}$, and $K_{4\mathrm{S}}$ are available in the supplementary material. Notice that the above formulation makes sense only between local sunrise ($\hat{t}_{\mathrm{SR}}$) and sunset ($\hat{t}_{\mathrm{SS}}$) times, that is,

$$K_{\mathrm{dir}} = \begin{cases} \text{Eq. (11)}, & \hat{t}_{\mathrm{SR}} < \hat{t} < \hat{t}_{\mathrm{SS}} \quad \text{(daytime)}. \\ 0, & -12h \le \hat{t} \le \hat{t}_{\mathrm{SR}} \ \text{ or } \ \hat{t}_{\mathrm{SS}} \le \hat{t} \le 12h \quad \text{(nighttime)}. \end{cases} \tag{12}$$

Hence Equation (11) is not yet a daily-periodic function valid over the whole daily cycle. The latter can be obtained through a Fourier series expansion:

$$K^*_{\mathrm{dir}}(\hat{t}) = K^*_0 + \sum_{m=1}^{\infty}\left[K^*_{m\mathrm{C}}\cos(m\omega\hat{t}) + K^*_{m\mathrm{S}}\sin(m\omega\hat{t})\right], \tag{13}$$

where an asterisk reminds us that these coefficients pertain to the series expansion valid over the whole daily cycle, whereas the homonymous ones in Equation (11) are valid for daytime only. These coefficients are computed as

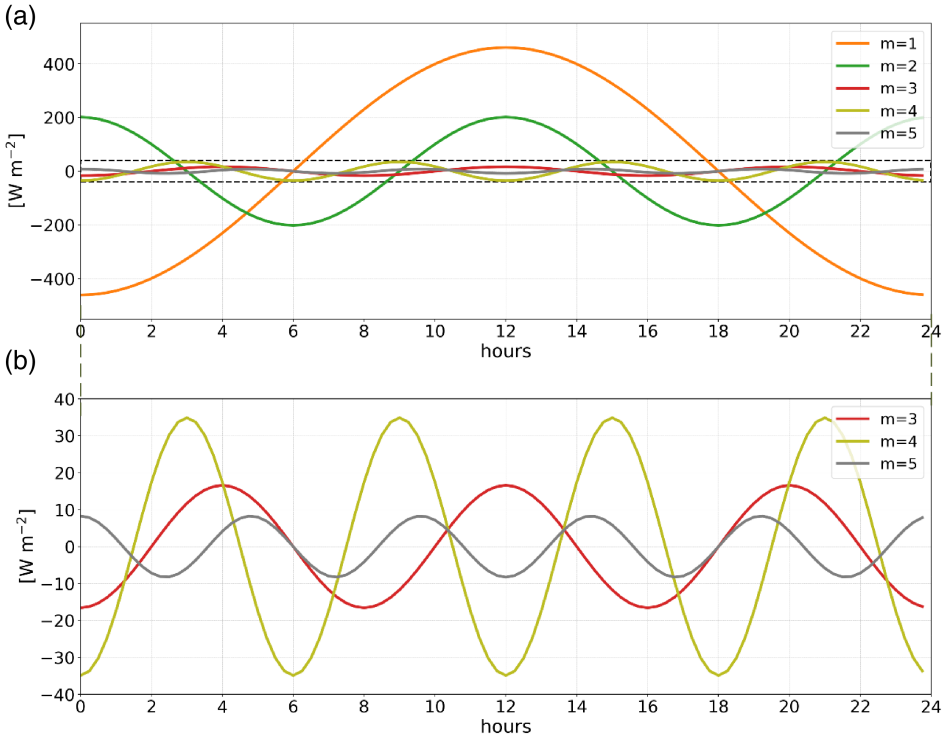

FIGURE 3 Single harmonics up to the fifth order for the summer solstice (DOY = 172), in the midlatitudes ($\phi = 45°$), for a steep south-facing slope ($\alpha = 45°$, $\gamma = 0°$). (a) shows all the harmonics, while (b) expands on the harmonics from the third order (between dashed lines in (a).

usual by

$$K_0^* = \frac{1}{T}\int_{\hat{t}_{SR}}^{\hat{t}_{SS}} K_{dir}(\hat{t})\, d\hat{t},$$
$$K_{mC}^* = \frac{2}{T}\int_{\hat{t}_{SR}}^{\hat{t}_{SS}} K_{dir}(\hat{t})\cos(m\omega\hat{t})\, d\hat{t},$$
$$K_{mS}^* = \frac{2}{T}\int_{\hat{t}_{SR}}^{\hat{t}_{SS}} K_{dir}(\hat{t})\sin(m\omega\hat{t})\, d\hat{t}, \quad (14)$$

where $T = 2\pi/\omega = 24$ h is the day duration. Notice that the lower and upper integration extremes are sunrise and sunset times, instead of −12 h and +12 h, respectively, as outside this range the incoming solar radiation is zero. The full form of the above coefficients can be found in the supplementary material.

Figures 3 and 4 show the performance of a truncated series expansion (Equation 13) in reproducing the full incoming radiation (Equation 12) and suggest that two harmonics may be sufficient for an acceptably accurate approximation, as higher-order harmonics exhibit an amplitude smaller than the first two by at least an order of magnitude.

In particular, Figure 4 shows how the sum of the different harmonics presented in Figure 3 (colored lines) reproduces the incoming radiation as in Equation (12) (solid black curve). Figure 4b,c offers an expanded view of the phases prior to sunrise and around solar noon respectively. Including more harmonics results in a signal closer to the reference curve. However, including up to the second-order harmonic already limits the discrepancy to about 40 W·m^{-2}, both for nighttime and for the peak at solar noon.

Even more so, the root-mean-square error (RMSE) with respect to the reference model (Equation 9) computed for various harmonics up to the 10th order (Figure 5) confirms that including harmonics of order higher than the second only reduces the discrepancy slightly, whereas harmonics higher than the fourth bring an almost negligible improvement. Anyway, for the sake of completeness and transparency, a code to compute the RMSE for any prescribed number of harmonics is available at the link indicated in the Data Availability Statement.

2.3 | Diffuse incoming radiation

Radiation that is diffused within the atmosphere is of particular importance over mountainous terrain, as slopes are often shaded from direct solar radiation there, but still receive some diffuse radiation. To account for the diffuse radiation, we adopt the expression proposed by Gates (1980), Kumar *et al.* (1997), and Seyednasrollah *et al.* (2013):

$$K_{dif} = SVF\, R_s \tau_D \cos Z \cos^2(\alpha/2), \quad (15)$$

where SVF is the sky-view factor, τ_D is the atmospheric diffusion factor, and $\cos^2(\alpha/2)$ is a factor accounting for the slope effect on the amount of skylight reaching

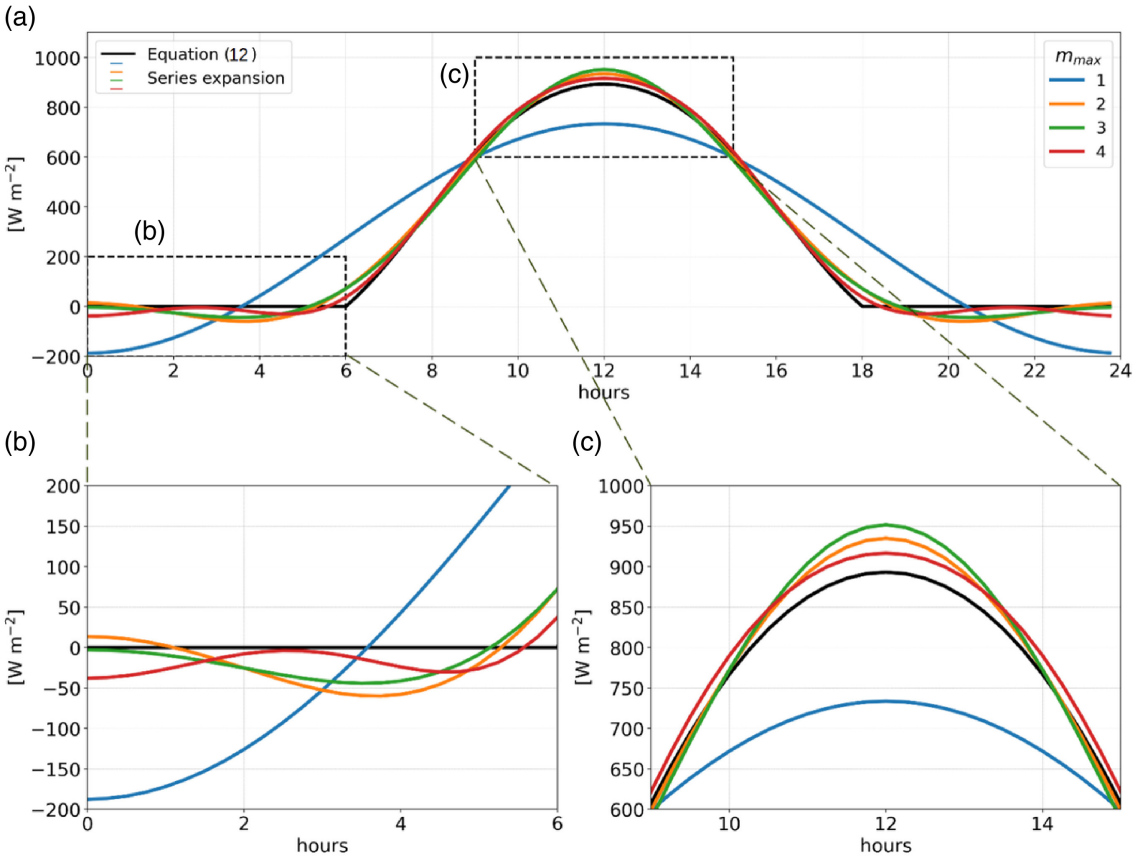

FIGURE 4 Performance of Equation (13) (colored lines) in reproducing the daily cycle of incoming solar radiation (Equation 12, black line), including an increasing number of harmonics for the same situation as in Figure 3. (a) Entire daily cycle, (b) nighttime, and (c) solar noon.

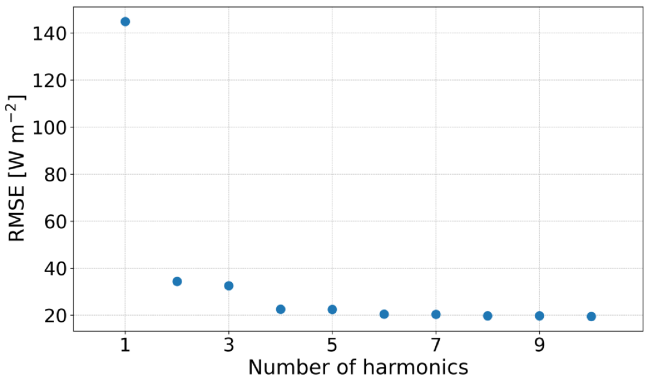

FIGURE 5 RMSE as a function of the number of harmonics included in the expansion for the same situation as in Figures 3 and 4.

the tilted plane. Since we are considering isolated, widely extended slopes here, we assume $SVF = 1$. Under clear-sky conditions, following Seyednasrollah *et al.* (2013), the atmospheric diffusion factor can be considered a linear function of the atmospheric transmittance: $\tau_D = a - b\tau$, with $a = 0.312$ and $b = 0.304$. Substituting τ from Equation (8), $\cos Z$ from Equation (7), and R_s as in Equation (4), Equation (15) can be rearranged to obtain

$$K_{dif}(\hat{t}) = K_{D0} + K_{D1C}\cos(\omega\hat{t}) + K_{D2C}\cos(2\omega\hat{t}) + K_{D3C}\cos(3\omega\hat{t}) + K_{D4C}\cos(4\omega\hat{t}). \quad (16)$$

The full expressions for the coefficients K_{D0}, K_{D1C}, K_{D2C}, K_{D3C}, and K_{D4C} are reported in the supplementary material.

Again, Equation (16) is valid between sunrise $\hat{t}_{SR_H}$ and sunset $\hat{t}_{SS_H}$ times evaluated for horizontal terrain:

$$K_{dif} = \begin{cases} \text{Eq. (17)}, & \hat{t}_{SR_H} < \hat{t} < \hat{t}_{SS_H} \quad \text{(daytime)}. \\ 0, & -12h \le \hat{t} \le \hat{t}_{SR_H} \text{ or } \hat{t}_{SS_H} \le \hat{t} \le 12h \quad \text{(nighttime)}. \end{cases} \quad (17)$$

Similarly to Equation (12), we evaluate a (truncated) Fourier series expansion of Equation (17) to obtain a daily periodic signal for the diffuse radiation:

$$K^*_{\mathrm{dif}}(\hat{t}) = K^*_{\mathrm{D0}} + \sum_{m=1}^{\infty} \left[K^*_{\mathrm{DmC}} \cos\left(m\omega\hat{t}\right) + K^*_{\mathrm{DmS}} \sin\left(m\omega\hat{t}\right) \right], \tag{18}$$

where again an asterisk denotes coefficients pertaining to the series expansion valid over a 24-h period. The coefficients can be calculated with similar formulations to those in Equation (14), but replacing the formulation of K_{dir} with the one for K_{dif}, and with the integration limits being the sunrise and sunset times as calculated for flat terrain conditions ($\hat{t}_{\mathrm{SR}_H}$ and $\hat{t}_{\mathrm{SS}_H}$ respectively). The full expressions are reported in the supplementary material.

2.4 | Shortwave net radiation

Summing up direct and diffuse radiation and considering an average surface albedo, we get a formulation for the net daily-periodic shortwave radiation on a slope:

$$\begin{aligned} K^*_{\mathrm{net}}(\hat{t}) &= (1-A)\left(K^*_{\mathrm{dir}}(\hat{t}) + K^*_{\mathrm{dif}}(\hat{t})\right) \\ &= (1-A)\left(K^*_0 + K^*_{\mathrm{D0}}\right) \\ &\quad + (1-A)\sum_{m=1}^{\infty}\Bigg[\left(K^*_{m\mathrm{C}} + K^*_{\mathrm{DmC}}\right)\cos\left(m\omega\hat{t}\right) \\ &\quad + \left(K^*_{m\mathrm{S}} + K^*_{\mathrm{DmS}}\right)\sin\left(m\omega\hat{t}\right)\Bigg]. \end{aligned} \tag{19}$$

For consistency, the series expansion for the diffuse component will be truncated at the fourth harmonic, as for the direct one.

Observations show that surface albedo exhibits strong variability from place to place and also during the annual cycle (e.g., over areas covered with deciduous forests): it is usually lower during the summer months and higher in winter, with peaks when the surface is covered by fresh snow (Tomasi *et al.*, 2017). Here, estimates based on measurements from Canadian inland (Williamson *et al.*, 2016), and in particular on a grassland site ("tundra" in Williamson *et al.*, 2016) representative of high elevation vegetation, suggested use of an average value of 0.2.

2.5 | Longwave radiation

The outgoing longwave radiation flux can be computed by means of the Stefan–Boltzmann law, adapted for a gray body:

$$L_{\mathrm{out}} = -\epsilon_{\mathrm{s}}\sigma T_{\mathrm{s}}^4, \tag{20}$$

where the minus sign is consistent with the convention adopted here, ϵ_{s} is the soil emissivity, $\sigma = 5.67 \times 10^{-8}\,\mathrm{W{\cdot}m^{-2}\cdot K^{-4}}$ is the Stefan–Boltzmann constant, and T_{s} is the surface temperature. The soil emissivity depends on the type of soil, with values ranging from 0.95 for dry dark clay to approximately 1 for melting snow or ice (An *et al.*, 2017; Ebrahimi & Marshall, 2015).

Longwave radiation emitted by the atmosphere can be computed as graybody emission as well:

$$L_{\mathrm{in}} = \epsilon_{\mathrm{a}}\sigma T_{\mathrm{a}}^4, \tag{21}$$

where ϵ_{a} is the atmospheric emissivity and T_{a} is the near-surface air temperature (usually the temperature at 2 m above ground level). In the absence of any information concerning the vertical structure of the atmospheric temperature, the near-surface air temperature can be approximated by the surface temperature. This is a rather crude approximation, and it is made here to derive the daily cycle of net radiation without formulating any hypothesis on the thermal structure of the atmosphere. We want to reassure the reader that this assumption will be re-examined in Part 2, where some hypothesis on the temperature structure will be made, allowing the computation of the actual temperature at 2 m. The value of ϵ_{a} depends strongly on the atmospheric composition: for example, molecular oxygen and nitrogen exhibit very low emissivities, while water vapor behaves like an almost perfect blackbody, with emissivity close to 1 (e.g., Ebrahimi & Marshall, 2015). Hence many models proposed in the literature estimate ϵ_{a} from one or more atmospheric parameters, such as air temperature, relative humidity, and cloud cover (e.g., Ångström, 1918; Brunt, 1932; Lhomme *et al.*, 2007; Swinbank, 1963). Commonly, ϵ_{a} is treated as an effective emissivity (e.g., Unsworth & Monteith, 1975), depending on both the clear-sky emissivity (ϵ_{cs}) and cloud cover through the cloud factor F (Sedlar & Hock, 2009):

$$\epsilon_{\mathrm{a}} = \epsilon_{\mathrm{cs}} F. \tag{22}$$

Here, we focus on clear-sky conditions, when thermally driven winds typically develop. Accordingly, the cloud factor is set to $F = 1$. The clear-sky emissivity ϵ_{cs} can be estimated with different levels of complexity, and many methods allow computing it as a function of the near-surface air temperature (Idso & Jackson, 1969; Swinbank, 1963). Here we adopt the model proposed by Maykut and Church (1973) and assume a constant value $\epsilon_{\mathrm{cs}} = 0.7248$.

Finally, the amount of incoming longwave radiation reflected by the surface must be considered. Hence the overall expression for the net longwave balance turns out to be

$$\begin{aligned} L_{\mathrm{net}} &= \epsilon_{\mathrm{cs}}\sigma T_{\mathrm{a}}^4 - \left[\epsilon_{\mathrm{s}}\sigma T_{\mathrm{s}}^4 + (1-\epsilon_{\mathrm{s}})\epsilon_{\mathrm{cs}}\sigma T_{\mathrm{a}}^4\right] \\ &= \epsilon_{\mathrm{s}}\epsilon_{\mathrm{cs}}\sigma T_{\mathrm{a}}^4 - \epsilon_{\mathrm{s}}\sigma T_{\mathrm{s}}^4 \approx -\epsilon_{\mathrm{s}}\sigma(1-\epsilon_{\mathrm{cs}})T_{\mathrm{s}}^4. \end{aligned} \tag{23}$$

Equation (23) allows connection of the daily cycle of surface net longwave radiation to the daily cycle of the

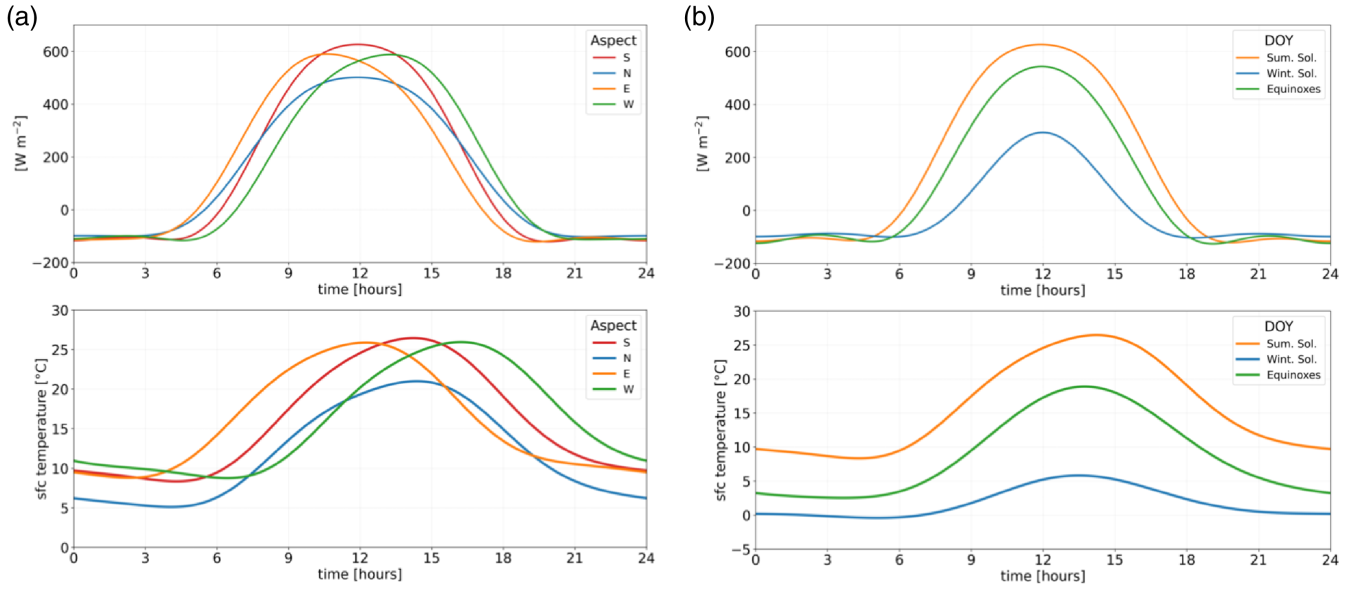

FIGURE 6 The upper panels show the daily cycle of net radiation as a function of (a) the day of the year and (b) slope orientation, obtained with the truncated Fourier series expansion. In the left panels, the daily cycles are calculated for DOY=172 (summer solstice), $\phi = 45°$, $\alpha = 10°$, and $h = 1500$ m. In the right panels, they are computed for $\phi = 45°$, $\alpha = 10°$, and $\gamma = 0°$. The number of harmonics used to produce the results is 4. The daily cycles of surface temperature used to compute the net longwave balances are shown in the lower panels.

surface temperature, which can be represented as a Fourier series expansion:

$$T_S(\hat{t}) = < T > + \sum_{m=1}^{\infty} \Delta T_m \sin(m\omega\hat{t} + \phi_m), \qquad (24)$$

where $< T >$ represents the daily mean, while ΔT_m and ϕ_m are the amplitude and phase of the mth harmonic respectively. The values of ΔT_m and ϕ_m can be obtained only by solving the surface energy budget, as will be explained in Part 2 of the present work. Here, we will set amplitude and phase to reasonable values to get realistic daily cycles of surface temperature for demonstration purposes only. Consistently with the solar radiation analysis, four harmonics will be considered to get the daily-periodic oscillations of temperature. The next subsection provides examples of the application of the model.

2.6 | Examples of application of the model

Figure 6 shows two radiation cycles produced by the model (upper panels) for different slope orientations and days of the year, resulting from an approximated daily cycle of surface temperature (lower panels). The latter are chosen as outlined in the previous paragraph, with phases and amplitudes allowing a daily minimum shortly before sunrise and a maximum slightly after the peak of incoming radiation. In Part 2 of the present article, amplitudes and phases will be derived by solving the surface energy budget.

3 | DISCUSSION AND CONCLUSIONS

A simplified analytical model for the estimation of the daily-periodic cycle of net radiation, including the diffuse component, locally valid for virtually any slope has been derived. The model estimates the daily-periodic cycle of total incoming radiation by means of (truncated) Fourier series expansions of well-established relationships and taking into account local terrain characteristics. The net radiation budget is obtained by estimating the net longwave radiation at the surface as a function of the daily cycle of surface and near-surface temperature.

The model is suited for slopes of any angle ($0° \leq \alpha \leq 90°$) and orientation ($0° \leq \gamma \leq 360°$), at any latitude and elevation (up to 2500 m), and provides an accurate estimate of the daily incoming solar radiation, taking into account astronomical relationships for extraterrestrial radiation and computing atmospheric transmittance from a simplified version of Hottel's model (Hottel, 1976). The relative absolute error in the total (integrated) incoming solar radiation is less than 2% compared with Hottel's formulation, which is of the order of magnitude of the maximum discrepancy claimed by Hottel (1976) with respect to values computed by integrating the solar radiation data from measurements.

The series expansion model for the incoming solar radiation (Equation 13) was tested to evaluate its performance in reproducing the reference signal (Equation 12) using the RMSE obtained including an increasing number of harmonics. Results show that including harmonics up to the second order is enough to reproduce the daily incoming solar radiation with acceptable accuracy. In fact, harmonics of order higher than the second have an amplitude at least one order of magnitude smaller than the first two, resulting in minor additions in the final shape of the daily-periodic signal. However, it should be noticed that the performance of the present model was evaluated with respect to a reference model (Equation 12). A better assessment could be made by comparing data from measurements.

The outgoing shortwave radiation was parameterized by means of a representative surface albedo, and the net longwave radiation was computed through the approximation of the surface (and near-surface) temperature by four daily-periodic harmonics, representing the daily cycle around a prescribed mean. Strictly speaking, the analytical constraints for computing the daily cycle of surface temperature can be rigorously derived only by solving the surface energy budget explicitly. Indeed, this will be done in Part 2 of the present article, for the particular case of thermally driven slope wind systems. Here, the test of the 24-h periodic analytical model for net radiation shows how it is capable of providing realistic estimates of the daily-periodic net radiation under clear-sky conditions for different days of the year and surface orientations, but can also be easily applied for different slope angles.

Overall, the proposed model provides a valuable tool to compute easily suitable input values for all processes controlled by the surface radiation budget. Therefore, it can be used as a "virtual net radiometer", providing a reference daily cycle of net surface radiation on a slope over the whole day, covering both nighttime and daytime for typical clear-sky days. This is particularly valuable in mountainous areas, where the installation and maintenance of radiometers is difficult, and pointwise measurements are usually not representative of the surroundings due to inclination and shading effects. Such a virtual net radiometer can be the basic input for estimating surface energy budgets, including sensible, latent, and ground heat fluxes, in view of deriving the daily evolution of surface temperature. In fact, the radiation-driven temperature can explain the observed remarkable differences between daytime heating and nighttime cooling regimes of slopes. In turn, this imbalance may control the onset and characteristics of boundary-layer flows typical of mountain areas (Zardi & Whiteman, 2013). However, the mechanisms by which the radiative budget controls the surface temperature and the onset of thermally driven flows will be investigated fully in Part 2.

In the present formulation, the model covers the simple case of a single isolated slope: future improvements could also take into account the shading effects induced by the surrounding topography. In fact, they can be of fundamental importance to the significant variety of local radiation microclimates that are frequently observed in complex terrain areas (Arthur *et al.*, 2018; Colette *et al.*, 2003; Whiteman *et al.*, 1989). Moreover, this variety of local effects on radiation may have an impact on the type of vegetation, thus also controlling the local albedo and the latent heat flux. To serve this purpose, the model can be easily implemented in a module for a geographic information system platform for pointwise estimation of clear-sky net radiation (Laiti *et al.*, 2014).

Finally, the current formulation and the coefficients used in the model proposed by Hottel (1976) for atmospheric transmittance assume a clear atmosphere with a visibility of 23 km. This might not be the case in all situations. In fact, when atmospheric conditions are different from the ideal (e.g., the presence of cloud cover or higher aerosol loads), the amount of solar radiation reaching the surface is reduced, and different coefficients for the atmospheric transmittance model need to be considered (Hottel, 1976). Therefore, future improvements of the present model should account for aerosol load in the atmosphere and cloud coverage (Grigiante *et al.*, 2011; Laiti *et al.*, 2018). These improvements might be addressed under the forthcoming field campaigns envisaged in the international research cooperation initiative TEAMx - Multi-scale transport and exchange processes in the atmosphere over mountains - programme and experiment (Rotach *et al.*, 2022; Serafin *et al.*, 2018).

ACKNOWLEDGEMENTS

M. Marchio acknowledges support from the Italian Ministry for University and Research (MUR) under the grant "Dipartimenti di Eccellenza (2018–2022)", awarded to the Department of Civil, Environmental and Mechanical Engineering of the University of Trento. S. Farina acknowledges support from the C3A–Center Agriculture Food Environment of the University of Trento and from Consorzio Difesa delle Produzioni Agricole Trento (Co.Di.Pr.A.). D. Zardi acknowledges support from the Italian Ministry for University and Research under the project "DECIPHER–Disentangling mechanisms controlling atmospheric transport and mixing processes over mountain areas at different space- and timescales" funded by the scheme "Research Projects of Relevant National Interest–Call 2022 (PNRR2022)", CUP E 53 D 23004450006, Protocol 2022NEWP4J.

CONFLICT OF INTEREST STATEMENT

The authors declare no conflict of interest.

DATA AVAILABILITY STATEMENT

Data sharing not applicable to this article as no datasets were generated or analysed during the current study. Python functions used in the article are available on Google Drive, in a folder accessible via the link: https://drive.google.com/drive/folders/1h2fmcfrmIScIJmlg4kr3mxNDeAY-3jDH?usp=sharing.

ORCID

Mattia Marchio https://orcid.org/0000-0003-4027-8958

REFERENCES

Allen, R.G., Trezza, R. & Tasumi, M. (2006) Analytical integrated functions for daily solar radiation on slopes. *Agricultural and Forest Meteorology*, 139, 55–73. Available from: https://doi.org/10.1016/j.agrformet.2006.05.012

An, N., Hemmati, S. & Cui, J.Y. (2017) Assessment of the methods for determining net radiation at different time-scales of meteorological variables. *Journal of Rock Mechanics and Geotechnical Engineering*, 9, 239–246. Available from: https://doi.org/10.1016/j.jrmge.2016.10.004

Ångström, A. (1918) *A study of the radiation of the atmosphere*, Vol. 65. Washington, DC: Smithsonian Institute Miscellaneous Collections.

Arthur, R.S., Lundquist, K.A., Mirocha, J.D. & Chow, F.K. (2018) Topographic effects on radiation in the WRF model with the immersed boundary method: implementation, validation, and application to complex terrain. *Monthly Weather Review*, 146, 3277–3292. Available from: https://doi.org/10.1175/MWR-D-18-0108.1

Brunt, D. (1932) Notes on radiation in the atmosphere. *Quarterly Journal of the Royal Meteorological Society*, 58, 389–420. Available from: https://doi.org/10.1002/qj.49705824704

Castelli, M., Stöckli, R., Zardi, D., Tetzlaff, A., Wagner, J.E., Belluardo, G. et al. (2014) The HelioMont method for assessing solar irradiance over complex terrain: validation and improvements. *Remote Sensing of Environment*, 152, 603–613. Available from: https://doi.org/10.1016/j.rse.2014.07.018

Colette, A., Chow, F.K. & Street, R.L. (2003) A numerical study of inversion-layer breakup and the effects of topographic shading in idealized valleys. *Journal of Applied Meteorology*, 42, 1255–1272. Available from: https://doi.org/10.1175/1520-0450(2003)042<1255:ANSOIB>2.0.CO;2

De Wekker, S.F.J., Kossmann, M., Knievel, J.C., Giovannini, L., Gutmann, E.D. & Zardi, D. (2018) Meteorological applications benefiting from an improved understanding of atmospheric exchange processes over mountains. *Atmosphere*, 9, 371. Available from: https://doi.org/10.3390/atmos9100371

Ebrahimi, S. & Marshall, S.J. (2015) Parameterization of incoming longwave radiation at glacier sites in the Canadian Rocky Mountains. *Journal of Geophysical Research: Atmospheres*, 120, 12536–12556. Available from: https://doi.org/10.1002/2015JD023324

Emeis, S., Kalthoff, N., Adler, B., Pardyjak, E., Paci, A. & Junkermann, W. (2018) High-resolution observations of transport and exchange processes in mountainous terrain. *Atmosphere*, 9, 457. Available from: https://doi.org/10.3390/atmos9120457

Farina, S., Marchio, M., Barbano, F., di Sabatino, S. & Zardi, D. (2023) Characterization of the morning transition over the gentle slope of a semi-isolated massif. *Journal of Applied Meteorology and Climatology*, 62, 449–466. Available from: https://doi.org/10.1175/JAMC-D-22-0011.1

Farina, S. & Zardi, D. (2023) Understanding thermally driven slope winds: recent advances and open questions. *Boundary-Layer Meteorology*, 189, 5–52. Available from: https://doi.org/10.1007/s10546-023-00821-1

Garnier, B.J. & Ohmura, A. (1968) A method of calculating the direct shortwave radiation income of slopes. *Cover Journal of Applied Meteorology and Climatology*, 7, 796–800. Available from: https://doi.org/10.1175/1520-0450(1968)007<0796:AMOCTD>2.0.CO;2

Gates, D.M. (1980) *Biophysical ecology*. New York: Springer-Verlag.

Giovannini, L., Ferrero, E., Karl, T., Rotach, M.W., Staquet, C., Trini Castelli, S. et al. (2020) Atmospheric pollutant dispersion over complex terrain: challenges and needs for improving air quality measurements and modeling. *Atmosphere*, 11, 646. Available from: https://doi.org/10.3390/atmos11060646

Giovannini, L., Laiti, L., Serafin, S. & Zardi, D. (2017) The thermally driven diurnal wind system of the Adige Valley in the Italian Alps. *Quarterly Journal of the Royal Meteorological Society*, 143, 2389–2402. Available from: https://doi.org/10.1002/qj.3092

Grigiante, M., Mottes, F., Zardi, D. & de Franceschi, M. (2011) Experimental solar radiation measurements and their effectiveness in setting up a real-sky irradiance model. *Renewable Energy*, 36, 1–8. Available from: https://doi.org/10.1016/j.renene.2010.04.039

Hargreaves, G.H. & Samani, Z.A. (1982) Estimating potential evapotranspiration. *Journal of the Irrigation and Drainage Division*, 108, 223–230. Available from: https://doi.org/10.1061/JRCEA4.0001390

Hottel, H.C. (1976) A simple model for estimating the transmittance of direct solar radiation through clear atmospheres. *Solar Energy*, 18, 129–134. Available from: https://doi.org/10.1016/0038-092X(76)90045-1

Idso, S.B. & Jackson, R.D. (1969) Thermal radiation from the atmosphere. *Journal of Geophysical Research*, 74, 5397–5403. Available from: https://doi.org/10.1029/JC074i023p05397

Iqbal, M. (1983) *An introduction to solar radiation*. Cambridge, MA: Academic Press.

Kirkpatrick, A.T. & Winn, C.B. (1984) Spectral analysis of the effective temperature in passive solar buildings. *Journal of Solar Energy Engineering*, 106, 112–119. Available from: https://doi.org/10.1115/1.3267553

Kreith, F. & Kreider, J.F. (2011) *Principles of sustainable energy*. Boca Raton, FL: CRC Press.

Kumar, L., Skidmore, A.K. & Knowles, E. (1997) Modelling topographic variation in solar radiation in a GIS environment. *International Journal of Geographical Information Science*, 11, 475–497. Available from: https://doi.org/10.1080/136588197242266

Laiti, L., Andreis, D., Zottele, F., Giovannini, L., Panziera, L., Toller, G. et al. (2014) A solar atlas for the Trentino region in the Alps: quality control of surface radiation data. *Energy Procedia*, 59, 336–343. Available from: https://doi.org/10.1016/j.egypro.2014.10.386

Laiti, L., Giovannini, L., Zardi, D., Belluardo, G. & Moser, D. (2018) Estimating hourly beam and diffuse solar radiation in an alpine valley: a critical assessment of decomposition models. *Atmosphere*, 9, 117. Available from: https://doi.org/10.3390/atmos9040117

Lhomme, J.P., Vacher, J.J. & Rocheteau, A. (2007) Estimating downward long-wave radiation on the Andean Altiplano. *Agricultural and Forest Meteorology*, 145, 139–148. Available from: https://doi.org/10.1016/j.agrformet.2007.04.007

Lindauer, M., Schmid, H.P., Grote, R., Steinbrecher, R., Mauder, M. & Wolpert, B. (2017) A simple new model for incoming solar radiation dependent only on screen-level relative humidity. *Journal of Applied Meteorology and Climatology*, 56, 1817–1825. Available from: https://doi.org/10.1175/JAMC-D-16-0085.1

Marchio, M., Farina, S. & Zardi, D. (2024) An analytical model for daily-periodic slope winds. Part 2. Solutions. *Quarterly Journal of the Royal Meteorological Society*, 150(764), 3925–3941. Available from: https://doi.org/10.1002/qj.4787

Maykut, G.A. & Church, P.E. (1973) Radiation climate of Barrow Alaska, 1962-1966. *Journal of Applied Meteorology and Climatology*, 12, 620–628. Available from: https://doi.org/10.1007/BF00866433

Mokhtari, A., Noory, H. & Vazifedoust, M. (2018) Performance of different surface incoming solar radiation models and their impacts on reference evapotranspiration. *Water Resources Management*, 32, 3053–3070. Available from: https://doi.org/10.1007/s11269-018-1974-9

Rotach, M.W., Serafin, S., Ward, H.C., Arpagaus, M., Colfescu, I., Cuxart, J. et al. (2022) A collaborative effort to better understand, measure, and model atmospheric exchange processes over mountains. *Bulletin of the American Meteorological Society*, 103, E1282–E1295. Available from: https://doi.org/10.1175/BAMS-D-21-0232.1

Sedlar, J. & Hock, R. (2009) Testing longwave radiation parameterizations under clear and overcast skies at Storglaciären, Sweden. *The Cryosphere*, 3, 75–84. Available from: https://doi.org/10.5194/tc-3-75-2009

Senkova, A.V., Rontu, L. & Savijarvi, H. (2007) Parametrization of orographic effects on surface radiation in HIRLAM. *Tellus A: Dynamic Meteorology and Oceanography*, 59, 279–291. Available from: https://doi.org/10.1111/j.1600-0870.2007.00235.x

Serafin, S., Adler, B., Cuxart, J., De Wekker, S.F.J., Gohm, A., Grisogono, B. et al. (2018) Exchange processes in the atmospheric boundary layer over mountainous terrain. *Atmosphere*, 9, 102. Available from: https://doi.org/10.3390/atmos9030102

Serafin, S. & Zardi, D. (2011) Daytime development of the boundary layer over a plain and in a valley under fair weather conditions: a comparison by means of idealized numerical simulations. *Journal of the Atmospheric Sciences*, 68, 2128–2141. Available from: https://doi.org/10.1175/2011JAS3610.1

Seyednasrollah, B., Kumar, M. & Link, T.E. (2013) On the role of vegetation density on net snow cover radiation at the forest floor. *Journal Geophysical Research Atmospheres*, 118, 8359–8374. Available from: https://doi.org/10.1002/jgrd.50575

Swinbank, W.C. (1963) Long-wave radiation from clear skies. *Quarterly Journal of the Royal Meteorological Society*, 89, 339–348. Available from: https://doi.org/10.1002/qj.49708938105

Tomasi, E., Giovannini, L., Zardi, D. & de Franceschi, M. (2017) Optimization of Noah and Noah_MP WRF land surface schemes in snow-melting conditions over complex terrain. *Monthly Weather Review*, 145, 4727–4745. Available from: https://doi.org/10.1175/MWR-D-16-0408.1

Tscholl, S., Tasser, E., Tappeiner, U. & Vigl, L.E. (2021) Coupling solar radiation and cloud cover data for enhanced temperature predictions over topographically complex mountain terrain. *International Journal of Climatology*, 42, 4684–4699. Available from: https://doi.org/10.1002/joc.7497

Unsworth, M.H. & Monteith, J.L. (1975) Long-wave radiation at the ground I. Angular distribution of incoming radiation. *Quarterly Journal of the Royal Meteorological Society*, 101, 13–24. Available from: https://doi.org/10.1002/qj.49710142703

Urgnani, R., Finco, A., Chiesa, M., Marzuoli, R., Bignotti, L., Riccio, A. et al. (2022) Size-segregated aerosol fluxes, deposition velocities, and chemical composition in an alpine valley. *Atmospheric Research*, 268, 105995. Available from: https://doi.org/10.1016/j.atmosres.2021.105995

Whiteman, C.D. (2000) *Mountain meteorology: fundamentals and applications*. Oxford, UK: Oxford University Press.

Whiteman, C.D. & Allwine, K.J. (1986) Extraterrestrial solar radiation on inclined surfaces. *Environmental Software*, 1, 164–169. Available from: https://doi.org/10.1016/0266-9838(86)90020-1

Whiteman, C.D., Fritschen, L.J., Orgill, M.M. & Simpson, J.R. (1989) Deep valley radiation and surface energy budget microclimates. Part I: radiation. *Journal of Applied Meteorology and Climatology*, 28, 414–426. Available from: https://doi.org/10.1175/1520-0450(1989)028<0414:DVRASE>2.0.CO;2

Williamson, S.N., Copland, L. & Hik, D.S. (2016) The accuracy of satellite-derived albedo for northern alpine and glaciated land covers. *Polar Science*, 10, 262–269. Available from: https://doi.org/10.1016/j.polar.2016.06.006

Zardi, D. & Whiteman, C.D. (2013) Diurnal mountain wind systems. In: Chow, F., de Wekker, S. & Snyder, B. (Eds.) *Mountain weather research and forecasting. Springer Atmospheric Sciences*. Dordrecht: Springer.

Zhang, Y., Kong, Z., Yang, Z., Wang, L. & Duan, X. (2017) Surface pollen distribution from alpine vegetation in eastern Tibet, China. *Scientific Reports*, 7, 586. Available from: https://doi.org/10.1038/s41598-017-00625-7

Zonato, A., Martilli, A., Gutierrez, E., Chen, F., He, C., Barlage, M. et al. (2021) Exploring the role of rooftop urban mitigation strategies in thermal comfort and energy consumption. *Journal Geophysical Research Atmospheres*, 126, 23. Available from: https://doi.org/10.1029/2021JD035002

SUPPORTING INFORMATION

Additional supporting information can be found online in the Supporting Information section at the end of this article.

How to cite this article: Marchio, M., Farina, S. & Zardi, D. (2024) An analytical model for daily-periodic slope winds. Part 1: Surface radiation budget. *Quarterly Journal of the Royal Meteorological Society*, 150(764), 3911–3924. Available from: https://doi.org/10.1002/qj.4785

APPENDIX A. APPROXIMATION OF ATMOSPHERIC TRANSMITTANCE

The exponential term in Hottel's expression (Hottel, 1976) for atmospheric transmittance (Equation 7) can be approximated as

$$\exp\left(-\frac{k}{\cos Z}\right) \simeq \exp\left(-\frac{k}{\cos(\phi-\delta)}\right) \times \frac{1}{F_c}(c_1\cos Z + c_2\cos 2Z + c_3\cos 3Z + \cdots), \quad \text{(A1)}$$

where the normalization factor is

$$F_c = c_1\cos(\phi-\delta) + c_2\cos(2(\phi-\delta)) + c_3\cos(3(\phi-\delta)) + \cdots \quad \text{(A2)}$$

The coefficients $c_1, c_2, c_3, \ldots$ can be determined from a best-fit procedure under the following constraints required to ensure physical consistency.

1. The right-hand side (rhs) of Equation (A1) needs to be non-negative at any time:

$$c_1\cos Z + c_2\cos 2Z + c_3\cos 3Z + \cdots > 0 \quad \text{for} \quad \cos Z > 0 \text{ (i.e., } t_{SR} < t < t_{SS}). \quad \text{(A3)}$$

2. The rhs of Equation (A1) needs to be zero when $\cos Z = 0$, that is, at sunrise and sunset for horizontal terrains:

$$c_1\cos Z + c_2\cos 2Z + c_3\cos 3Z + \cdots = 0 \quad \text{for} \quad \cos Z = 0 \ (t = t_{SR}, t_{SS}). \quad \text{(A4)}$$

This implies that the coefficients of all the even harmonics need to be zero. Preliminary tests (shown below) with a simple iterative implementation of the procedure under various settings (days of the year, latitudes, and elevations) showed that three harmonics with appropriate coefficients may be enough to reproduce the complete exponential expression by means of the approximation in Equation (A1).

For an expansion truncated at the third harmonic, we can set $c_1 = 1$.

The physics of the problem requires a maximum at solar noon ($\hat{t} = 0$), which implies

$$-1 + 3c_3(1 - 4\cos^2(\phi-\delta)) \le 0. \quad \text{(A5)}$$

Three possible ranges of acceptable values of c_3 exist according to the value of $|\phi-\delta|$.

1. For $|\phi-\delta| > 60°$: the term in brackets is positive and the acceptable values for c_3 are

$$c_3 \le \frac{1}{3(1-4\cos^2(\phi-\delta))}. \quad \text{(A6)}$$

2. For $|\phi-\delta| < 60°$: the term in brackets is negative and the acceptable values for c_3 thus are

$$c_3 \ge \frac{1}{3(1-4\cos^2(\phi-\delta))}. \quad \text{(A7)}$$

3. For $|\phi-\delta| = 60°$: the term in brackets is zero, and the left-hand side (lhs) of Equation (A5) is negative for all values of c_3.

The performance of the above approximation (green curve) is compared in Figure A1 with the performance of the simplest approximation, obtained using $c_3 = 0$ in the reconstruction of the exponential term (lhs of Equation A1). The three case studies show that the single harmonic approximation underestimates the exponential term of Hottel (1976), while the inclusion of the third harmonic offers a better fit. The approximation using the best fit of c_3 seems to overestimate the exponential term slightly around sunrise and sunset.

To evaluate the error introduced by the above approximation, the relative error in the resulting integration of the daily cycle of the incoming solar radiation was computed. In particular, the relative error was computed as a function of the day of the year, for different values of latitude (Figure A2 left panel) and elevation (Figure A2 right panel), as they are present in the variables of the lhs of Equation (A1).

Figure A2 shows the improvement obtained by using three harmonics in the approximation of the exponential term. The single harmonic approximation underestimates the incoming solar radiation for almost all conditions, as a result of the underestimation of the exponential term in the atmospheric transmittance (as seen in Figure A1). This underestimation is particularly remarkable during the warm season, with a peak in summer, when the discrepancy between Hottel (1976) and the single harmonic approximation is larger. On the other hand, using a three-harmonics approximation results in the relative error oscillating, with a slight overestimation of the incoming radiation during the cold season and an underestimation during warm months. In any case, the relative error is bounded in the range ±2%, confirming the goodness of the model for the incoming solar radiation.

In the end, the resulting values of the c_3 coefficient from the best-fitting procedure, considering the conditions of Equations (A6) and (A7), for a combination of days of the year, latitudes, and elevations are shown in Figure A3. The best-fitting procedure was carried out allowing the algorithm to explore values from −10 up to the threshold value for $|\phi-\delta| < 60°$, from the threshold up to +10 for $|\phi-\delta| > 60°$, and from −10 to +10 for $|\phi-\delta| = 60°$ with a resolution of 0.001. In any case, as Figure A3 shows, the best-fitting values for c_3 are found to be in the range ±0.35.

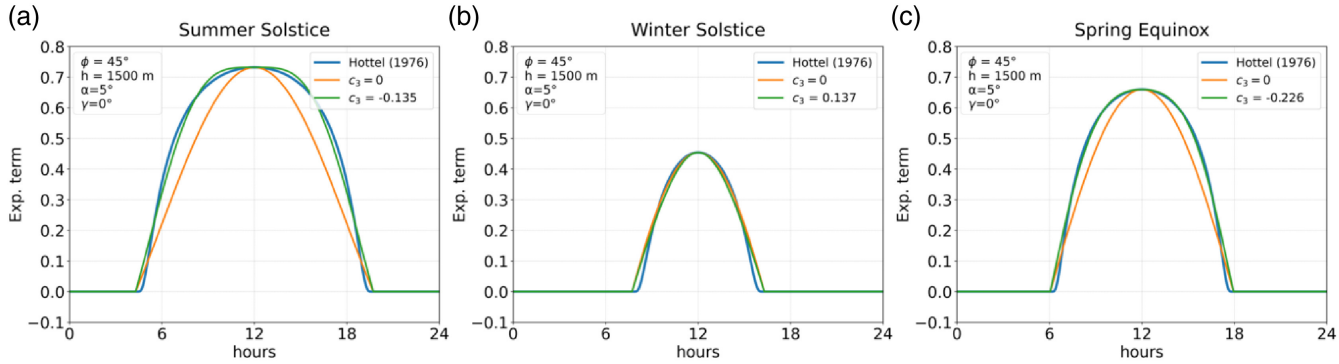

FIGURE A1 Comparison of the performance of the two approximations ($c_3 = 0$ and c_3 from best fit, respectively) in approximating the exponential term present in the formulation of the atmospheric transmittance by Hottel (1976). Case studies: summer and winter solstices and one of the equinoxes. Fixed parameters for all case studies are $\phi = 45°$, $\alpha = 5°$, $\gamma = 0°$, and $h = 1500$ m. Blue and green curves are almost superimposed.

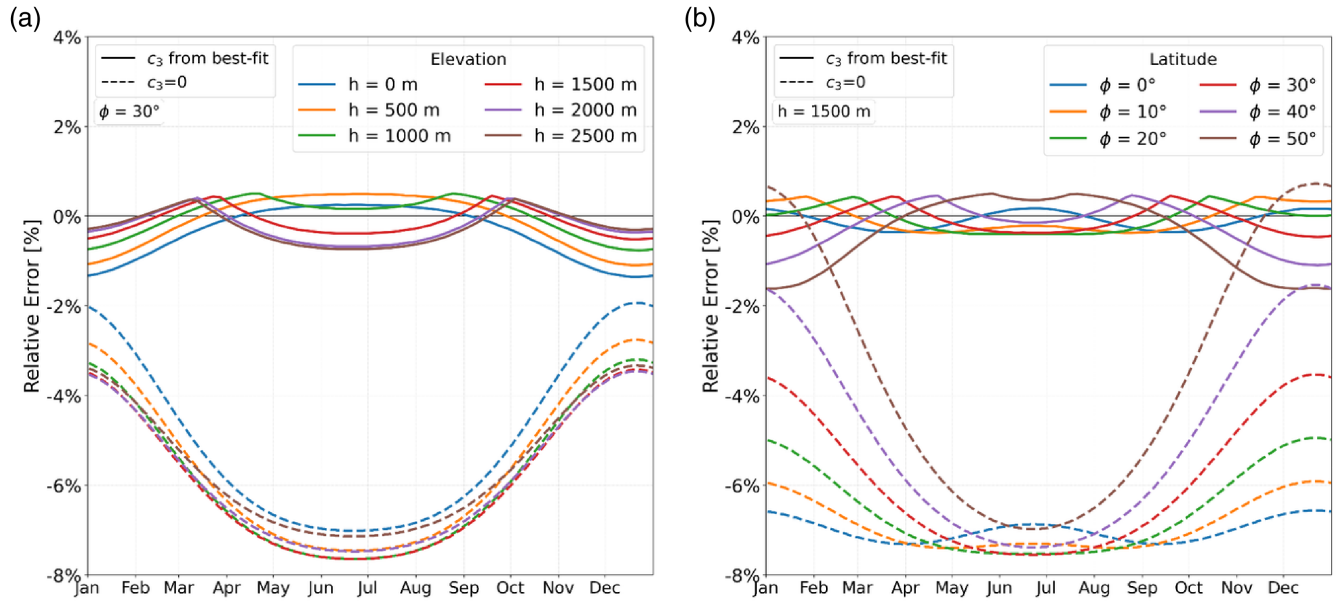

FIGURE A2 Relative error on the total daily radiation by using the approximated atmospheric transmittance as in Equation (A1) with respect to the incoming solar radiation computed using Hottel's (1976) model for all days of the year for different elevations above sea level (left) and latitudes (right).

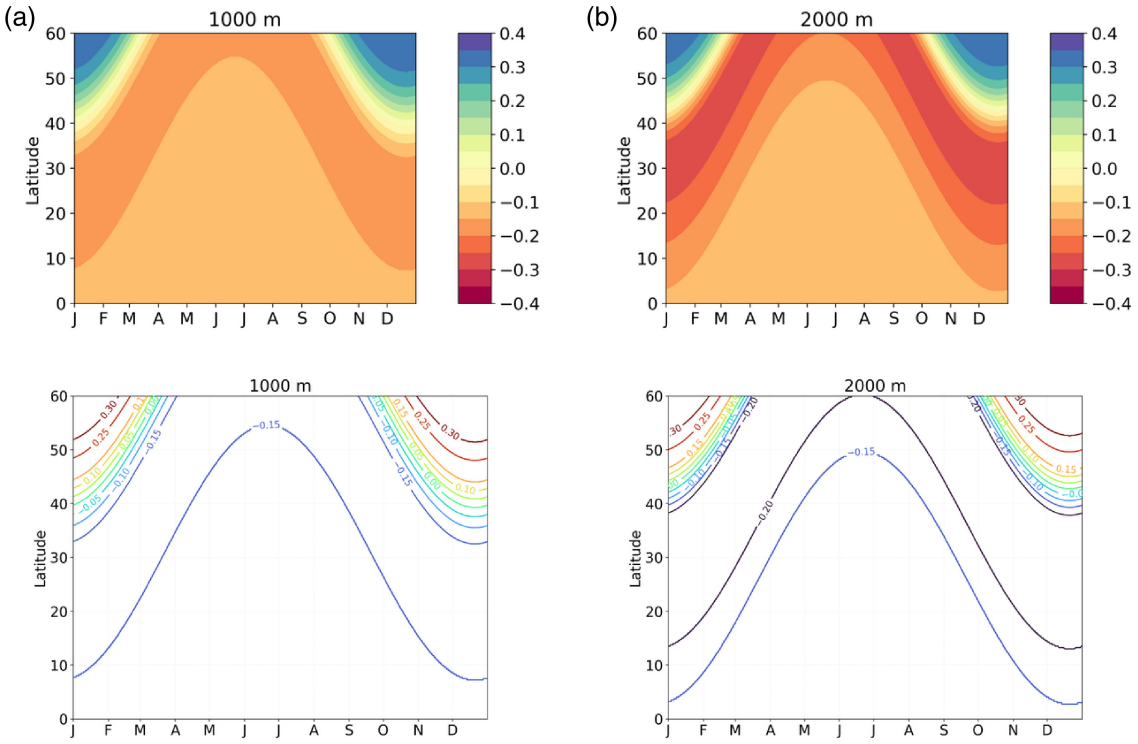

FIGURE A3 Values of c_3 coefficient from best-fit as a function of the day of the year and latitude for two sets of elevations: (a) h = 1000 m, and (b) h = 2000 m.